Ammonium Bifluoride-Etched MXene Modified Electrode for the All—Vanadium Redox Flow Battery

Maedeh Pahlevaninezhad,[a] Rad Sadri,[a] Damilola Momodu,[a] Karamullah Eisawi,[b] Majid Pahlevani,[c] Michael Naguib,[b] and Edward P. L. Roberts*[a]

The development of electrodes with high performance and long-term stability is crucial for commercial application of vanadium redox flow batteries (VRFBs). This study compared the performance of VRFB with thermal-treated and MXene-modified carbon paper. To prepare the MXene, a modified-etching process with ammonium—bifluoride (NH_4HF_2) led to a mild and efficient conversion of the MAX-phase to MXene compared to etching process with hydrofluoric-acid (HF). Electron microscopy and X-ray diffraction studies revealed that the etching process with NH_4HF_2 led to MXene nanostructures with a large interlayer spacing. The results show that at a current density of 60 mA cm^{-2}, the energy efficiency increased by 25.5% when using a NH_4HF_2 -etched MXene-modified negative electrode, by 12.5% with a thermal-treated MXene-modified electrode, and by 4% with an HF-etched MXene-modified electrode, in comparison to the pristine electrode. The maximum power density of the battery was increased by more than 40%. In long-term cycling experiments the MXene modified electrode exhibited excellent stability over 1000 cycles of charge-discharge, with 0.05% discharge capacity decay per cycle, amongst the lowest values reported to date and four times lower than for thermally-treated electrode. The superior performance was linked to the improved electrical conductivity and wettability, higher interlayer spacing, and lower charge transfer resistance for the V^{2+}/V^{3+} redox reaction.

Introduction

The vanadium redox flow battery (VRFB) is the most intensively studied redox flow battery (RFB) technology, and commercial VRFBs are available for large-scale energy storage systems (ESS).[1–3] In an RFB, the electrical energy is stored using dissolved redox active species within the liquid electrolyte. The electrolytes are pumped through the porous electrodes in the cell, which are separated by a membrane to prevent cell short-circuit and mixing of the anolyte with the catholyte.[4,5] Using the vanadium redox active species as a single element in VRFBs eliminates electrolyte cross-contamination, which is one of the main issues in other RFB chemistries. Compared to other battery technologies for ESS, VRFBs offer advantages including independent power (stack size) and energy (electrolyte), long lifetime, high round trip efficiencies, design flexibility, scalability, no cross-contamination, low environmental impact and no fire hazards.[4,6] Although the VRFB is the most developed of RFBs due to its advantages, the VRFB still suffers from notable problems like low energy and power densities compared to the other battery technologies.[7–13] To overcome these challenges, the VRFB must be operated at high current density during charge-discharge without forfeiting the battery performance. It should also be noted that as the operating current density increases, the polarization losses also increase, including the charge transfer, ohmic, and concentration losses.[14] This leads to a decrease in the battery efficiency at high current density. The electrode is one of the main battery components that directly affects battery power. The VRFB electrodes provide the active surface area,[4,13] and influence the charge transfer and concentration polarization for the redox reactions, which are crucial to the overall battery performance.[14,15] Carbon and graphite felts have been widely used as VRFB electrode materials,[16] however the restricted active sites accessible for redox reactions and the low fiber volume fraction ($<8\%$) leads to relatively poor electrochemical activity.[17] On the other hand, alternative electrode materials like carbon papers with higher fiber volume provides efficient electron transport and reduce resistance losses in the battery due to larger fraction of redox reaction sites. Therefore, a combination of carbon paper materials with structured flow fields could increase the VRFB's power output.[16,18,19] Currently, VRFBs mostly use carbon-based materials for the electrode due to its high stability, low cost, corrosion resistance, and good electrical conductivity. However, the battery performance can be enhanced by improving the

[a] Dr. M. Pahlevaninezhad, Dr. R. Sadri, Dr. D. Momodu, Prof. E. P. L. Roberts
Department of Chemical and Petroleum Engineering, University of Calgary, 2500 University Dr NW, Calgary, AB T2N 1N4, Canada
E-mail: edward.roberts@ucalgary.ca
Homepage: https://profiles.ucalgary.ca/edward-roberts

[b] K. Eisawi, Assoc. Prof. M. Naguib
Department of Physics and Engineering Physics, Tulane University, New Orleans, LA 70118, United States
Homepage: https://sse.tulane.edu/pep/faculty/naguib

[c] Assoc. Prof. M. Pahlevani
Department of Electrical and Computer Engineering, Queen's University, 99 University Avenue, Kingston, Ontario, K7L 3N6, Canada
Homepage: https://smithengineering.queensu.ca/directory/faculty/majid-pahlevani

Batteries & Supercaps

Research Article
doi.org/10.1002/batt.202300473

Chemistry Europe
European Chemical
Societies Publishing

electrochemical activity of the electrodes characteristics.[4,15] Different modification methods have been proposed and applied to enhance performance.

Surface treatment, decoration with electro-catalysts, and surface etching techniques have been successfully applied for electrode modification.[14] Common examples of surface treatment methods include thermal,[16,20,21] chemical,[22,23] plasma,[24] and electrochemical modification.[25] Thermal treatment is one of the widely used methods to enhance the electrode activity by increasing wettability and oxygen functionalization of the surface.[16] One of the first studies of the thermal treatment of electrodes for VRFB applications was reported by Skyllas-Kazacos et al. in 1992.[26] They obtained a 10% improvement in the VRFB charge-discharge energy efficiency due to the formation of C=O and C−O−H functional groups as the active sites on the electrode surface.[26] Researchers have also investigated various nanostructured metal- and carbon-based electrocatalysts to improve the VRFB performance.[27–30] Because the mechanism of the positive and negative redox reactions differs, the electrocatalysts needed for each reaction may be different. Previous studies have shown that 80% of the cell overpotentials are related to the V^{2+}/V^{3+} redox reaction at the negative electrode.[31] Therefore, the development of an effective electrocatalyst for the V^{2+}/V^{3+} redox reaction at the negative reaction is critical.[32]

MXene, a large family of two-dimensional (2D) transition metal carbides, carbonitrides and nitrides,[33] with high conductivity and hydrophilicity is a promising candidate as an electro-catalyst for VRFBs.[34,35] $Ti_3C_2T_x$ (T_x stands for mixed surface terminations) was the first[36] and most widely studied MXene for a range of applications.[34,37–39] A few studies of the use of HF (hydrofluoric acid)-etched MXene's for VRFB have been reported. Wei et al.[14] studied the application hollow $Ti_3C_2T_x$ MXene spheres as an electrocatalyst for the V^{2+}/V^{3+} redox reaction in a VRFB. They applied a multi-step process including polymer sphere synthesis and an annealing treatment to modify graphite felt with MXene. It was found that at a current density of 200 mA cm^{-2}, the charge-discharge energy efficiency was increased by 15.7% compared to a pristine (untreated) graphite felt electrode, while exhibiting stable cycling.[14] Jing et al.[40] explored the effect of ionic liquid etched and microwave-assisted delaminated MXene as an electrocatalyst on the carbon fiber for the VRFB application. They achieved 7.53% higher energy efficiency compared to the pristine carbon fiber at a current density of 200 mA cm^{-2} and the discharging capacity was found to decrease by around 0.12% per cycle. Mizrak et al.[41] investigated the effect of HF-etched MXene on the anodic reaction in VRFB by using a simpler modification of the negative electrode. They obtained an increase in energy efficiency of 17% at a current density of 100 mA cm^{-2}, although the stability of the electrode was not studied.[41]

Selective etching using strong acids,[36,42,43] which are highly toxic and corrosive has been the most common way to etch Al from the MAX phase Ti_3AlC_2 to form $Ti_3C_2T_x$ MXene. However, this method presents significant hazards, has issues with colloidal instability and requires multi-step rinsing processes.[44]

In this study, we aim to explore the potential of ammonium bifluoride (NH_4HF_2)-etched $Ti_3C_2T_x$ MXene as a novel electrocatalyst for the modification of electrode in VRFBs. To the best of our knowledge, there have been no prior studies that have reported the use of NH_4HF_2-etched MXene for VRFB applications. This innovative approach involves utilizing NH_4HF_2 for etching MXene and subsequently applying the etched MXene to modify electrodes for VRFBs. By adopting this novel method, we replace hazardous etchants with NH_4HF_2, offering a milder and safer alternative in comparison to conventional strong acids such as HF.[45] The ammonium-intercalated $Ti_3C_2T_x$ MXene can be exfoliated by direct ultrasonication to form stable few-layered nanosheets in aqueous or organic solvents. In addition, NH_4HF_2-etched MXene has been reported to exhibit a larger interlayer spacing compared to those etched with other etchants, such as HF.[46,47] This larger interlayer spacing facilitates the diffusion of electrolyte ions into the electrode,[48] holding promising implications for improved battery performance. For comparison, HF-etched MXene was synthesised and applied as an electrocatalyst for the V^{2+}/V^{3+} redox couple to compare the VRFB performance with NH_4HF_2-etched MXene modified electrode. Comprehensive electrochemical studies including cyclic voltammetry (CV), electrochemical impedance spectroscopy (EIS), battery polarization, charge-discharge at different current density, and long duration cycling were performed. Based on the polarization results, adopting thermally treated electrodes decorated with MXene nanostructures on the anodic side, yielded a device that could operate at much higher current densities which significantly increased the VRFB power density. As a result, the modified electrodes could offer a significant enhancement in the battery performance while reducing the battery stack size for a specific power requirement. The NH_4HF_2-etched MXene demonstrated excellent properties such as high hydrophilicity and electrical conductivity from a low cost and environmentally friendly route which makes it a good candidate for VRFB application.

Experimental

Material

Titanium (Ti, −325 mesh, 99% purity), aluminum (Al, −325 mesh, 99.5% purity), and graphite (C, 7–11 μm, 99% purity) were purchased from Alfa Aesar. A solution of 1.6 M vanadium oxysulfate ($VOSO_4$) dissolved in 3 M sulfuric acid, prepared in deionized (DI) water (>18.2 MΩ cm), was used as the electrolyte. $VOSO_4$ (99.5% purity) was purchased from NOAH Technologies while, H_2SO_4 (95–98% purity) and ammonium bifluoride (NH_4HF_2, >99.99% purity) were obtained from Millipore Sigma. Carbon paper electrode (Sigracet 39AA, 280 μm thickness, pore size 43 μm) and Nafion 117 membrane were purchased from Ion Power, Inc.

Synthesis of Ti_3AlC_2 MAX phases and $Ti_3C_2T_x$ MXene

The synthesis of Ti_3AlC_2 MAX phases was performed by mixing the elemental powders of titanium, aluminum, and graphite with a molar ratio of Ti: Al: C = 3: 1.2: 1.88. The powders were added to a high-density polyethylene (HDPE) bottle with 10 yttria stabilized

zirconia (YSZ) balls of 10 mm diameter. Then, they were mixed by rotation at 56 rpm for 3 h using a Turbula T2F mixer. The furnace heating was conducted by loading the mixed powders in an alumina crucible placed in the center of an alumina tube furnace at 1600 °C for 2 h under a continuous flow of argon (Ar) at a rate of 0.2 L min^{-1}. A heating rate of 10 °C min^{-1} was used throughout the heating process. The heated mixture was left to cool down to room temperature inside the furnace. The synthesized Ti_3AlC_2 phase was ground, and the resulted powder was sieved to obtain particle size less than 45 μm.

$Ti_3C_2T_x$ was synthesized by selective etching of Al layers from the parent Ti_3AlC_2 MAX phase. The etching process was performed using an aqueous solution of ammonium bifluoride (NH_4HF_2). A mass of 1 g of Ti_3AlC_2 powder was slowly added to a 40 ml solution of 2 M NH_4HF_2 due to the exothermic nature of the reaction. Thereafter, The Ti_3AlC_2/NH_4HF_2 mixture was stirred at 400 rpm for 48 h at 50 °C. After the reaction process, the acquired MXene was repeatedly washed with DI water using an ultrahigh centrifuge (Sorvall Legend X1R, Thermo Scientific, Germany) at 3500 rpm in 10 mins intervals until a neutral pH was obtained. Further, the materials were treated in 0.5 M NaOH solution for 3 h and then washed with DI water several times. Simultaneously, the ammonium intercalated MXene was centrifugally separated from the supernatant and vacuum dried at 40 °C for 12 h.

To delaminate the MXene nanosheets, 250 mg of the ammonium-intercalated MXene was suspended in 50 ml of DI water using a water bath Sonicator (Bransonic® CPXH 2800-E, Branson Ultrasonics Corporation, USA) under flowing Argon for 60 min. Ice cubes were successively placed in the sonication bath to keep the water temperature at 5 °C. This was followed by centrifugation for 10 min at 2500 rpm. Then, the supernatant comprising a stable dispersion of delaminated MXene flakes in DI water was collected for electrode modification.

In addition to NH_4HF_2 etching, MXene was also synthesized using HF etching for comparison. The HF etching method is described in Section S1 (see Supplementary Information), following a method reported in the literature.[49]

MXene modified electrode preparation

To fabricate the ammonium-intercalated $Ti_3C_2T_x$-modified electrode, Sigracet 39AA carbon paper substrates were cut into 5 cm^2 rectangular sheets. The carbon papers were initially washed by isopropyl alcohol immersion for 20 min to remove traces of organic impurities before vacuum drying. Subsequently, they were thermally treated at 500 °C for 1 h under air.

A 5 mg ml^{-1} MXene dispersion obtained after delamination was drop-cast on both sides of the thermally treated carbon paper electrode using a pipette, and the electrode was then dried in a vacuum oven at 50 °C for 1 h. The drop-casting/drying process was repeated until a loading of MXene of 1 mg cm^{-2} (determined from the mass change of the dried electrode) was obtained for each electrode prior to incorporation in the VRFB for battery testing.

MXene modified electrode characterization

Scanning electron microscopy (SEM, Quanta FEG-250, Thermo-Fisher Scientific, USA) studies of the electrode before and after modification were conducted to examine the morphology of the electrode. To explore and confirm the structure of the MXene modified electrode, X-ray diffraction (XRD) analysis was conducted using a diffractometer (Bruker D8 Advance ECO, LYNXEYE XE

detector, Bruker AXS INC, USA) equipped with Cu Kα source (λ 1.54178 Å, 25 mA, 40 kV).

X-ray photoelectron spectroscopy (XPS) analysis was performed with a VG ESCALAB 220i XL, (Thermo Scientific, USA) to investigate the surface chemistry of the electrodes and measure their elemental compositions. XPS is a surface-sensitive analytical technique that provides information about the surface chemistry and electronic state of materials. XPS detection was used to confirm the chemical composition, bonding form, and elemental valence on the surface of the synthesized MXene. A JEOL JEM-ARM200F analytical TEM (at 200 kV, JEOL USA Inc.) was used to investigate the surface morphology of the MXene modified electrode. Finally, contact angle measurements were conducted with a Ramé-Hart Contact Angle Goniometer (Ramé-Hart Instrument Co., Succasunna, NJ). The contact angle of a 2 μL water droplet was determined by image analysis. As soon as the water droplet was placed on the electrodes surface, the contact angle was measured to avoid evaporation effects.

Cyclic Voltammetry

A three-electrode setup was used for CV analysis to evaluate the electrochemical characteristics of the electrode. Carbon paper (geometric area of 0.18 cm^2, pristine, thermally treated at 500 °C in air for 1 h, thermally treated and modified with NH_4HF_2-etched or HF-etched MXene), a Pt wire (Pine Research Instrumentation, Inc. USA), and a silver/silver chloride (Ag/AgCl) electrode were used as the working, counter, and reference electrode, respectively. The solution was purged with nitrogen gas for 20 min to deoxygenate the electrolyte before each CV experiment, and a nitrogen blanket was applied during the measurements. A potentiostat (BioLogic VSP) was used to control the potential during CV experiments, using a potential window of 0 V to −0.7 V versus Ag/AgCl in order to study the V^{2+}/V^{3+} redox reaction.

VRFB flow cell testing

VRFB charge-discharge experiments were performed using a flow cell (5 cm^2 effective area, supplied by Fuel Cell Technology Inc.) with a serpentine flow field. Thermally treated carbon paper (at 500 °C in air for 1 h) was used as the positive electrode, and either pristine, thermally treated, or thermally treated and MXene modified carbon paper was used as the negative electrode. A Nafion 117 membrane was used to separate the two electrodes. Although cells using carbon paper have been reported to have a lower power density than those using carbon or graphite felt, and alternative membrane materials can also offer higher performance,[3,14] the objective of this study is not to optimize the cell design or maximize the VRFB performance. Like-for-like comparison of MXene modified electrode materials using the same cell design and electrode substrate enable investigation of the impact of the etching method on the VRFB cell behavior.

Figure 1. illustrates the schematic of the VRFB flow cell. The negative and positive electrolyte tanks were initially filled with 20 ml and 40 ml of 1.6 M vanadium oxysulfate ($VOSO_4$) dissolved in 3 M H_2SO_4 electrolyte, respectively. This difference in volume is required since two electrons are transferred to complete charging of the V^{4+} in the negative electrolyte (V^{4+}/V^{2+}), while for the positive electrolyte only one electron is transferred (V^{4+}/V^{5+}). Thus, the volume of the positive electrolyte should be doubled to maintain the charge balance in both tanks. The cell was charged at constant current until the cell voltage reached a cutoff voltage of 1.65 V, then the cell voltage was kept constant at 1.65 V until the applied current decreased to below 1 mA. Then, 20 ml of the
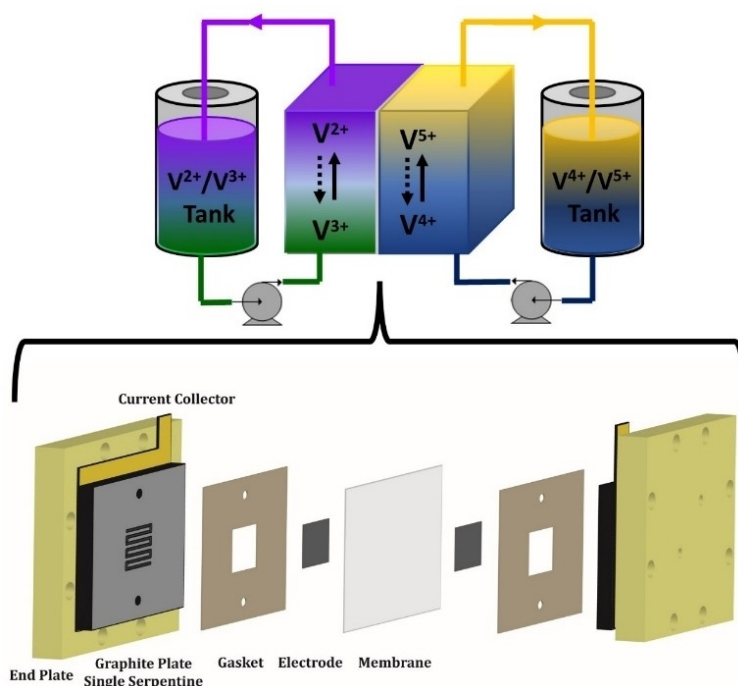
Figure 1. Schematic design of the VRFB charge-discharge cell.

positive electrolyte was removed from the tank prior to starting charge-discharge experiments. A dual-head peristaltic pump (Masterflex, Cole Parmer) was used to circulate the electrolyte solutions through the cell with flow rate of 20 ml min^{-1}. The membrane was soaked for 24 h in DI water in order to prepare the membrane for use in the flow cell.[6,50] To remove oxygen from the electrolyte solution, nitrogen was continuously bubbled through the electrolytes for 30 min before, and during, the charge-discharge experiments. The charge-discharge experiments were performed at current densities in the range 10 to 120 mA cm^{-2}, using cut-off voltages of 1.65 V during charge, and 0.8 V for discharge. For the charge-discharge experiments, a potentiostat (BioLogic VSP with VMP3B-20 booster) operating in galvanostatic mode was used. The VRFB performance including coulombic efficiency (CE), voltage efficiency (VE), and energy efficiency (EE) were determined based on the following equations (1) to (3):[6,51]

$$CE = \frac{Q_d}{Q_c} \times 100\%$$ (1)

$$VE = \frac{V_{d,avg}}{V_{c,avg}} \times 100\%$$ (2)

$$EE = CE \times VE$$ (3)

where Q_c and Q_d are the charge and discharge capacities (in mA h), respectively; and $V_{c,avg}$ and $V_{d,avg}$ are the average voltages during charge and discharge.

For the polarization and EIS experiments, the state of charge (SOC) of the battery was adjusted to 50%, corresponding to an open circuit voltage of around 1.4 V.[52] The galvanostatic polarization was performed with a 30 second hold per step to obtain a steady state cell potential. The cell was recharged at 25 mA/cm^2 back to a 50% SOC after each step in the polarization. For the polarization experiments, a potentiostat (BioLogic VSP with booster VMP3B-20)

was used. EIS was conducted at open circuit potential, in the frequency range from 100 kHz to 1 mHz.

Results and discussion

MXene modified electrode characterization

The XRD analysis of Ti$_3$AlC$_2$ MAX phase, NH$_4$HF$_2$-etched MXene, and HF-etched MXene are shown in Figure 2a. The characteristic peaks at 2θ values of 9.54°, 19.15°, 34.11°, 36.80°, 39.01°, 41.79°, 44.92°, 48.48°, 52.50°, 56.49° and 60.27° are assigned to the (002), (004), (101), (103), (104), (105), (106), (107), (108), (109), and (110) planes of Ti$_3$AlC$_2$ MAX phase, respectively.[53] From the XRD results, it is evident that the etching process has a noticeable impact on the structural order and crystallinity of the MAX phase. The intense diffraction peaks corresponding to (104) at approximately 38.8° are nearly absent in both the AB-etched and HF-etched MXene samples, indicating the successful removal of the Al layers from the MAX phase.[54] Furthermore, the (002) peak, which corresponds to the basal planes of the two-dimensional titanium carbide layers, displays a clear downward shift from $2\theta = 9.56°$ to $2\theta = 8.85°$ and $2\theta = 7°$ in HF-etched MXene and NH$_4$HF$_2$-etched MXene, respectively, which is linked to the larger d-spacing caused by the structural expansion during etching and substitution of Al layers with terminating groups like —F, —OH/=O.[46] Additionally, the c lattice parameter[45] which is the spacing between the layers in the MXene structure exhibits an increase from approximately 18.5 to 20 Å in HF-etched MXene and approximately 25 Å in NH$_4$HF$_2$-etched MXene layers, consistent with previous findings.[47,55] These findings indicate that the use of NH$_4$HF$_2$ etchant with the
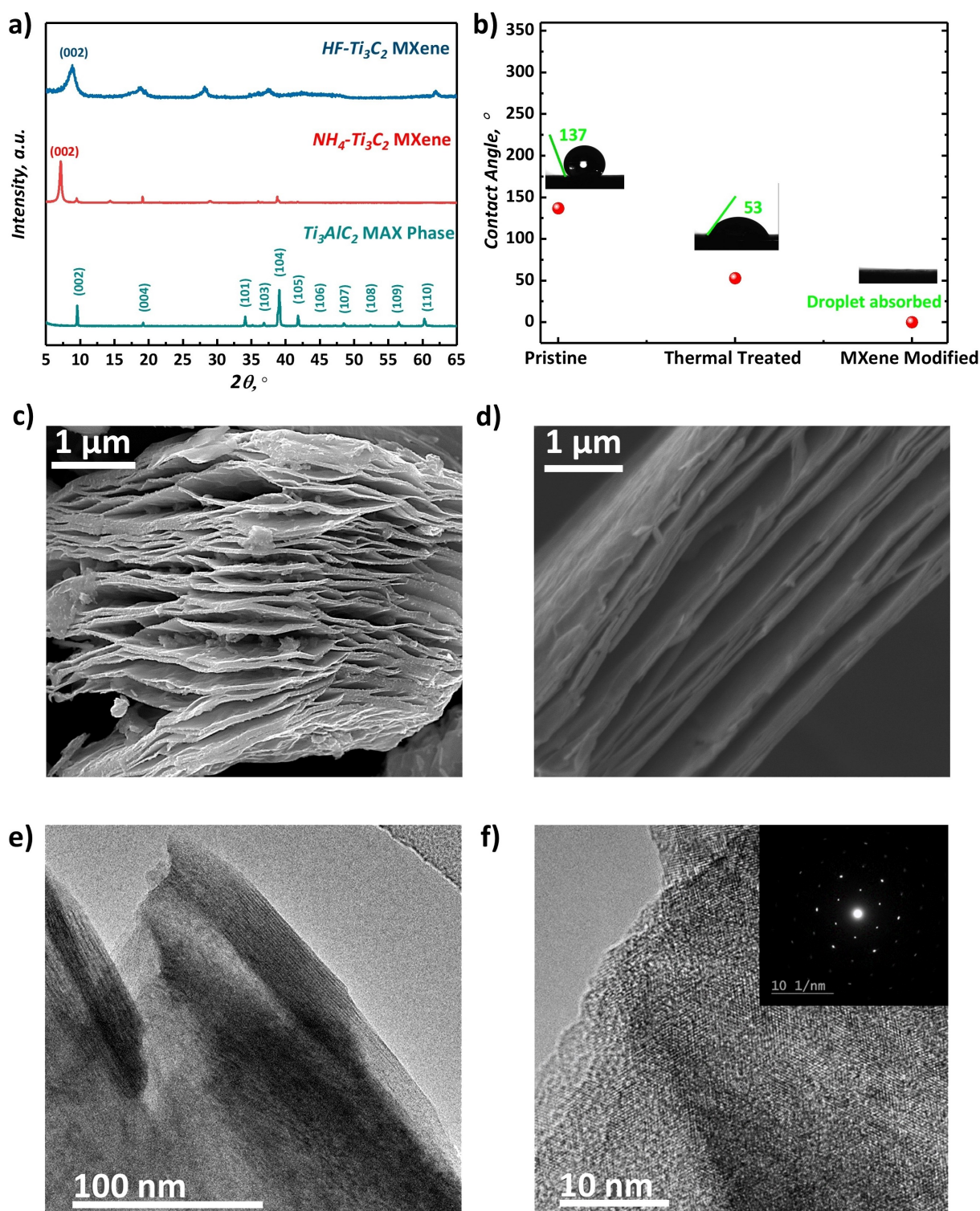
Batteries & Supercaps

Research Article
doi.org/10.1002/batt.202300473

Chemistry Europe
European Chemical
Societies Publishing

Figure 2. (a) XRD results for Ti$_3$AlC$_2$ MAX phase, NH$_4$HF$_2$-etched MXene, and HF-etched MXene; (b) Static water contact angle on different electrodes. (c) SEM images of NH$_4$HF$_2$-etched MXene electrode material; (d) SEM images of HF-etched MXene electrode material; (e) TEM image of NH$_4$HF$_2$-etched MXene showing Ti$_3$C$_2$T$_x$ MXene nanostructures (f) high magnification TEM image of NH$_4$HF$_2$-etched MXene with figure inset showing the SAED pattern.

Ti$_3$AlC$_2$ precursor leads to a larger interplanar spacing in MXene nanostructures due to higher cation size (radius) of etchant when compared to that obtained with HF.

Figure 2b. shows the electrode's wettability based on the static contact angle. The wettability of porous electrodes affects electrolyte diffusion and access to the active sites on the electrode surface. Thus, improving electrode hydrophilicity is one of the crucial factors for enhancing VRFB performance.[41] The contact angle for the pristine electrode was 137°. After thermal treatment the wettability of the carbon paper in-

Batteries & Supercaps

Research Article
doi.org/10.1002/batt.202300473

**Chemistry
Europe**
European Chemical
Societies Publishing

creased, with a 53° contact angle, consistent with previous studies.[16,21] The MXene-coated electrode surface was found to be hydrophilic, and rapidly absorbed the DI water droplet. It can be concluded that the hydrophilicity of the VRFB electrode was significantly enhanced by the presence of MXene on the carbon paper.

Figure 2c and 2d shows SEM micrographs of the exfoliated NH_4HF_2-etched MXene and HF-etched MXene, respectively. The separated sheets in Figure 2c clearly demonstrate that the ammonium salt was effective for Al-etching. The presence of the stacked/separated sheets with interlayer spacing provides exposed electrochemically active surfaces for ions during electrolyte flow and circulation. The SEM image of HF-etched MXene in Figure 2d confirms the successful etching of the MAX phase by HF. The lower spacing between the layers for the HF-etched MXene is evident in the SEM images. It is expected that the morphology of the intercalated MXene will look different from its non-intercalated counterpart.[46] The intercalation of species generated from the NH_4HF_2 etchant affects the morphology of the final MXene nanostructures.[46] NH_3 and NH_4^+ intercalates in the MAX structure leading to a MXene with thinner sheets and larger interlayer spacings, as observed from the XRD analysis. Due to the highly corrosive nature of HF, the layers begin to collapse and MXene sheets coalesce to form a more compact morphology with lower interlayer spacing, as shown in Figure 2d and from XRD analysis. On the other hand, the NH_3 and NH_4^+ intercalation combined with the less corrosive NH_4HF_2-etchant leads to a MXene with a more expanded structure and larger interlayer spacing. Figure S1. shows a comparison of the SEM images of the thermally treated and NH_4HF_2-etched MXene modified electrodes. Carbon paper is composed of smooth fibers and small flakes. In the case of thermally treated carbon paper, smooth fiber surfaces were

observed (Figure S1. a and b), while for the NH_4HF_2-etched MXene modified electrodes, the fiber surfaces and flakes were coated with the MXene sheets (Figure S1. c and d). The micrographs confirm a uniform MXene coating on the electrode surface.

The HRTEM images of NH_4HF_2-etched MXene flakes are shown in Figure S1.e and f, confirming the presence of thin and large exfoliated flake-like sheets with average lateral dimensions of 0.5–1 μm. The transparency of the sheets confirms the successful exfoliation into single or few layer MXene. The HRTEM images in Figure 2e and 2f clearly show the layered MXene microstructures with the presence of fringes evident from adjacent overlapping sheets. The presence of regular edges on the flakes confirms the mild nature of the etching process which yielding the relatively large flakes.[56] The inset to Figure 2f shows the selected area electron diffraction (SAED) pattern with clear bright spots forming hexagonal rings that further confirms the efficient delamination of sheets during the transformation of MAX phase to MXene.[56]

The wide survey XPS spectra illustrated in Figure 3a confirmed the presence of titanium and carbon elements. Meanwhile, the presence of additional fluorine, oxygen, and nitrogen in the etched sample resulted from the exfoliation of the MAX phase with NH_4HF_2. It is worth noting that the aluminum peak was not detected (Figure S2), which confirms the removal of Al with NH_4HF_2 using modified etching conditions for the synthesis. This is in contrast to the XPS spectra for HF-etched MXene,[57] for which the Al 2p peaks are detected. The Ti 2p, C 1s, O 1s, and F 1s region are common in both NH_4HF_2 and HF-etched samples, however as expected there is no N 1s peak with HF etching.

The Ti 2p spectra of the MXene nanolayers is illustrated in Figure 3b in which Ti 2p was fitted with a doublet separation
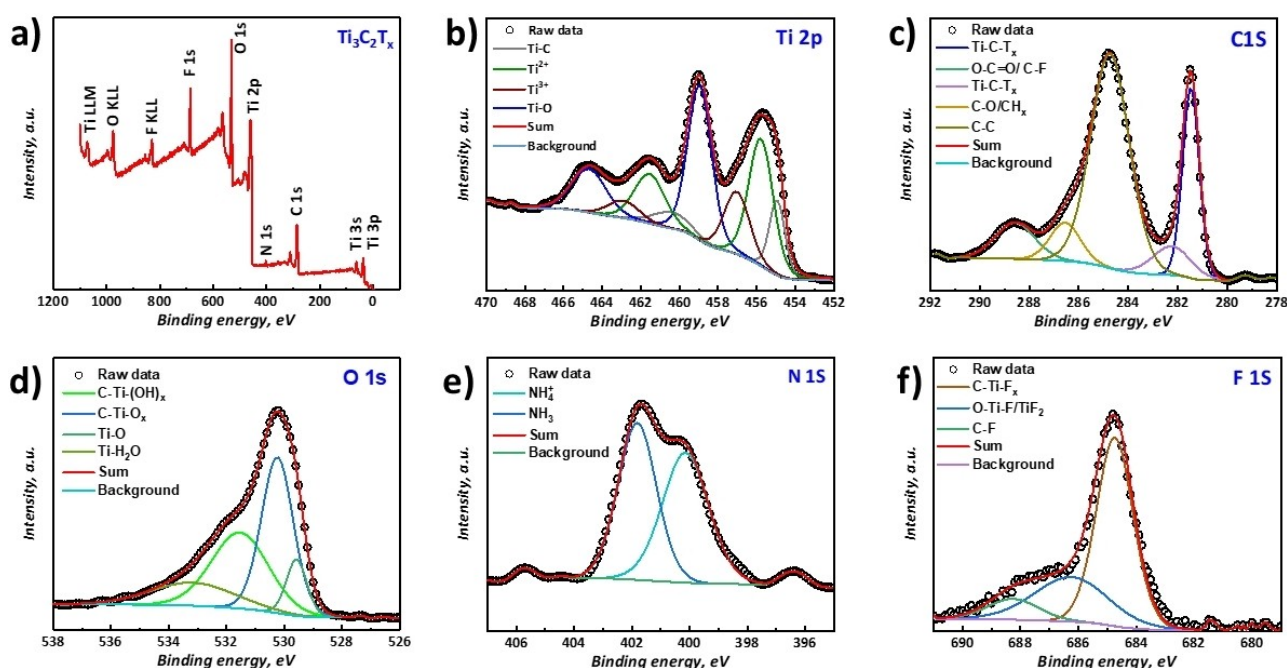

Figure 3. (a) XPS survey spectrum of NH_4HF_2-etched MXene; High resolution XPS survey spectrum for (b) Ti 2p; (c) C 1s, (d) O 1s; (e) N 1s; (f) F 1s.

Batteries & Supercaps

Research Article
doi.org/10.1002/batt.202300473

Chemistry Europe
European Chemical
Societies Publishing

including four doublets (Ti $2p^{3/2}$ and Ti $2p^{1/2}$). The Ti $2p3/2$ level is associated with the core electrons of the titanium atom, while the Ti $2p1/2$ level is associated with the valence electrons. The binding energies of Ti $2p^{3/2}$ for Ti–C, Ti^{2+}, Ti^{3+}, and Ti–O are about 454.9, 455.8, 457, and 459 eV, respectively, which are in harmony with the results in the literature.[14,58–61] It should be noted that the visible peaks corresponding to Ti–O reflect MXene's slight oxidation, but this does not affect its physicochemical properties or structure.

The Figure 3c presented the C 1s spectra fitted with five Gaussian-Lorentzian curves in which a sharp asymmetric peak at the low binding energy of ~281.8 eV[62] is associated with the carbon atoms that are bonded to Ti (i.e. C–Ti) in the Ti$_3$C$_2$ structure, which is fitted with two curves,[61,63] while the peak at 282.2 eV is attributed to the sp^2 hybridized carbon atoms (i.e. C–C) in the graphitic-like regions of the MXene flakes.[46,58,63,64] The other two peaks centered at ~286.6 and ~288.5 eV can be attributed to C–O/CH$_x$[58,63,64] and O–C=O[63]/C–F,[65] respectively. The oxygen-containing species are either adsorbed on the surface or incorporated into the MXene structure.

The O 1s spectra in Figure 3d can be fitted using seven components located at 529.5, 530.1, 531.8, and 533.3 eV, corresponding to surface species of Ti–O, C–Ti–O$_x$, C–Ti–(OH)$_x$, and H$_2$O, respectively which align with earlier studies.[64,66] The presence of hydroxyl functional groups that terminate the MXene surface contribute to the electrochemical activity for the vanadium redox reactions storage capacity.[67,68] The XPS spectra of the N 1s region in Figure 3e indicates the successful intercalation of NH$_3$ and NH$_4^+$ between the MXene layers.[46] The presence of NH$_4^+$ likely improves conductivity which aids storage kinetics within the battery. The F 1s region (Figure 3f) can be deconvoluted into C–Ti–F$_x$, O–Ti–F/TiF$_2$ and C–F bonds which are located at binding energies of 685,[65] 686.3[60] and 688.2 eV.[60,65]

Cyclic voltammetry

CV experiments were conducted and compared for four working electrodes: pristine, thermal treated, NH$_4$HF$_2$-etched and HF-etched MXene modified carbon paper, in order to evaluate the effect of MXene as an electrocatalyst for the anodic redox reaction (V^{2+}/V^{3+}). The CV curves obtained for the V^{2+}/V^{3+} redox couple in 1.6 M V$_2$(SO4)$_3$ and 3 M H$_2$SO$_4$ electrolyte are shown in Figure 4. For pristine carbon paper, no oxidation or reduction peaks were observed (Figure 4a), while the thermal treated and MXene modified electrodes improved the V^{2+}/V^{3+} redox reaction kinetics, consistent with previous studies.[6,14,40,41] The NH$_4$HF$_2$-etched MXene modified electrode demonstrated the highest kinetics for the V^{2+}/V^{3+} redox reaction based on the peak separation and peak current followed by HF-etched MXene modified and thermal treated electrodes. A peak separation (ΔE_p) of 152 mV, 132 mV, and 107 mV was recorded for the thermal treated, HF-etched MXene modified, and NH$_4$HF$_2$-etched MXene modified electrode, respectively. The peak currents for the NH$_4$HF$_2$-etched MXene modified electrodes were also observed to be significantly higher than thermal treated and HF-etched MXene modified electrode.

The CV data confirms an improved electrochemical activity due to the catalytic effect of MXene on the electrode surface coupled with the higher wettability. In addition, hydrogen evolution is known to be a parasitic side reaction common in the negative potential range.[6,69] The CV results show no evidence of hydrogen evolution in the negative potential window. Figure 4b. shows the CVs for NH$_4$HF$_2$-etched MXene modified electrode at a range of scan rates from 10 to 50 mV s^{-1}. A plot of the square root of scan rate versus cathodic and anodic peak currents (Figure S3) shows a linear relationship. This indicates that the V^{2+}/V^{3+} redox reaction is limited by diffusion at the electrolyte-electrode interface, rather than by charge transfer.

The results obtained are comparable with those reported previously for HF-etched MXene modified electrodes in
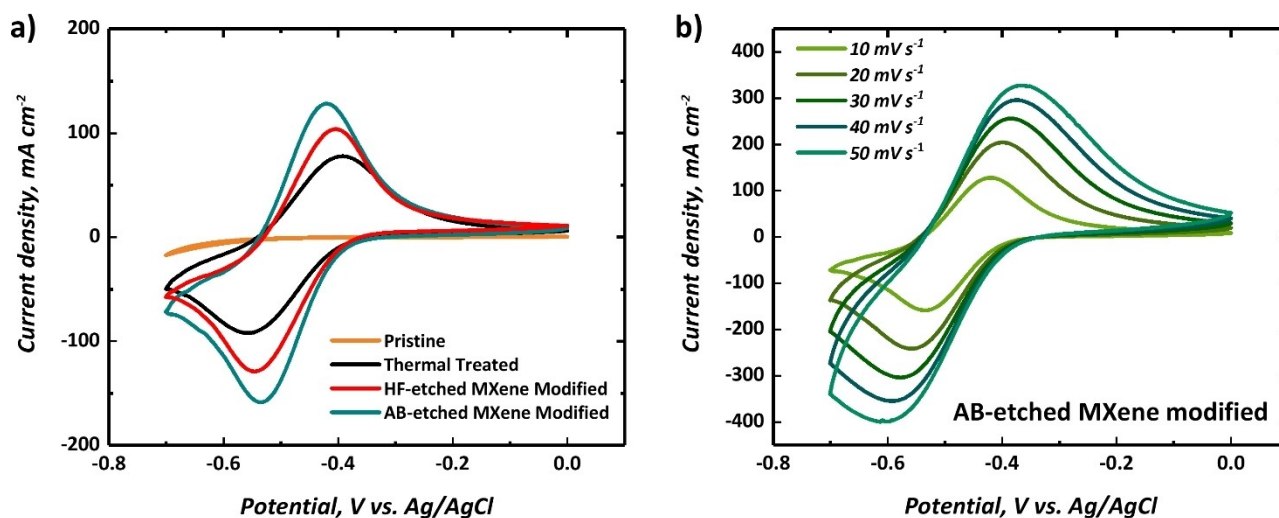

Figure 4. (a) Cyclic voltammetry for pristine, thermal treated, HF-etched and AB-etched (NH$_4$HF$_2$-etched) MXene modified electrodes at a scan rate of 10 mV s^{-1} for V^{2+}/V^{3+} in 1.6 M V$_2$(SO$_4$)$_3$ and 3 M H$_2$SO$_4$, (b) Cyclic voltammetry for AB-etched MXene modified electrode at different scan rates ranging 10 to 50 mV s^{-1}.

VRFB.[14,40,41] The higher peak current density and lower peak separation observed in this study suggests that the electrochemical activity of the NH_4HF_2-etched MXene modified electrode used was higher than previously reported.

VRFB flow-cell performance

To investigate the impact the NH_4HF_2-etched MXene modified negative electrode on the VRFB performance, charge-discharge, EIS, and polarization experiments were conducted using a flow cell. The flow cell performance was compared with a VRFB using a pristine and thermal treated carbon paper electrode as the negative electrode. The charge-discharge voltage curves versus capacity at a range of current densities from 10–120 mA cm^{-2} is presented in Figure S4, respectively. The discharge capacity of the VRFB using a NH_4HF_2-etched MXene modified negative electrode was the highest at all current densities, and the capacity enhancement increased with current density. At each current density, with the NH_4HF_2-etched MXene modified electrode, the cell voltage during charging was lower, and the cell voltage during discharge was higher than obtained with the bare carbon paper negative electrodes. This implies lower overpotential losses with the MXene modified electrode, allowing greater charge flow during charging and discharge before the cut-off cell voltages were reached. The lower overpotentials are related to the better wettability and electrocatalytic activity of the MXene nanostructures due to larger interlayer spacing, which provides more active sites on the electrode surface and better kinetic for the V^{2+}/V^{3+} redox reaction.

These results are consistent with the findings from the CV analysis. As the current density increased, the ohmic, charge transfer and mass transport overpotential losses in the flow cell are expected to increase.[6] As the charge-discharge was performed with a cut-off voltage protocol from 0.8 V to 1.65 V, the charge and discharge capacities thus decreased as the current density increased. The MXene modified electrode enabled an increase in the maximum possible operating current density using this cut-off voltage protocol, from 80 to 120 mA cm^{-2} due to lower overpotential during the charge-discharge cycle.

The battery efficiencies for pristine, thermally treated, and MXene modified electrode (etched with HF and NH_4HF_2: AB) at different current densities are summarized in Figure 5. The performance of the VRFB cell with the baseline carbon paper electrodes is similar to that reported in previous studies.[17,41] The coulombic efficiency as a function of varying current density (Figure 5a) show a similar increasing trend for all the electrodes to a coulombic efficiency of ~100% as the current density increased from 10 to 120 mA cm^{-2}. The increase in coulombic efficiency is linked to a decreased crossover of vanadium species as the charge-discharge time decreases with current density, leading to a higher coulombic efficiency.[6,41]

Figure 5b shows a decrease in the voltage efficiency of the VRFB with current density due to increasing ohmic, charge transfer, and mass transport overpotentials. The VRFB using a pristine carbon paper negative electrode had the lowest voltage efficiency, followed by those using the thermally treated, HF-etched, and NH_4HF_2-etched MXene modified electrodes. This reveals that the weak kinetics of the pristine carbon paper negative electrode limits the charge-discharge of the VRFB to current densities of 60 mA cm^{-2} or less. The thermal treatment of the electrode enhances the kinetics, enabling an increase in the maximum operating current density of the charge-discharge to 80 mA cm^{-2}. Modifying the negative electrode with MXene led to the highest voltage efficiency at all current densities, with a corresponding increase with current density. The lower overpotentials with the NH_4HF_2-etched MXene modified negative electrode further increased the maximum operating current density of the VRFB charge-discharge to 120 mA cm^{-2}. The VRFB energy efficiency (Figure 5c) follow the same trend as voltage efficiency due to the small variation of CE. The energy efficiency for the VRFB using the NH_4HF_2-etched MXene modified negative electrode was 81.5%, 77.5%, 72%, and 65% at current densities of 60, 80, 100, and 120 mA cm^{-2} respectively. The NH_4HF_2-etched MXene modification of the thermally treated negative electrode increased the energy efficiency by 12.5% and 17% at current densities of 60 and 80 mA cm^{-2}, respectively. The enhanced performance is linked to the high electrochemical activity of MXene nanostructure that facilitates electron transfer during the redox reactions, which improves the overall efficiency of the VRFB.

The discharge capacity decreased with current density as expected, due to increased overpotential losses (Figure 5d). The discharge capacity of the VRFB using a NH_4HF_2-etched MXene modified negative electrode had the highest capacity in all cases. For example, the discharge capacity at a current density of 60 mA cm^{-2} for the NH_4HF_2-etched MXene modified, HF-etched MXene modified, thermally treated, and pristine electrodes were 539, 460, 336, and 99 mA h, respectively. The discharge capacity of HF-etched MXene modified, thermally treated, and pristine electrodes was 17%, 38% and 82% less than MXene modified electrode at a current density of 60 mA cm^{-2}. The theoretical capacity for the 1.6 M vanadium with 20 ml volume is 857.6 mA h. The discharge capacity of the NH_4HF_2-etched MXene modified electrode was around 63% of the theoretical capacity at a current density of 60 mA cm^{-2}, and only 39% of the theoretical capacity in the case of thermally treated electrode. Thus, the NH_4HF_2-etched MXene modification of the negative electrode led to a large increase in electrolyte utilization.

A comparative analysis between the HF-etched MXene modified electrode and the NH_4HF_2-etched MXene modified electrode reveals a slight increase of approximately 5% in both voltage efficiency and energy efficiency across all current densities. Notably, when considering a current density of 80 mA cm^{-2}, the NH_4HF_2-etched MXene modified electrode exhibits a 30% higher discharge capacity compared to the HF-etched MXene modified electrode. This enhancement can be attributed to the larger interlayer spacing of the NH_4HF_2-etched MXene, which facilitates improved transportation of vanadium ions to and from the electrode. Consequently, this enhanced
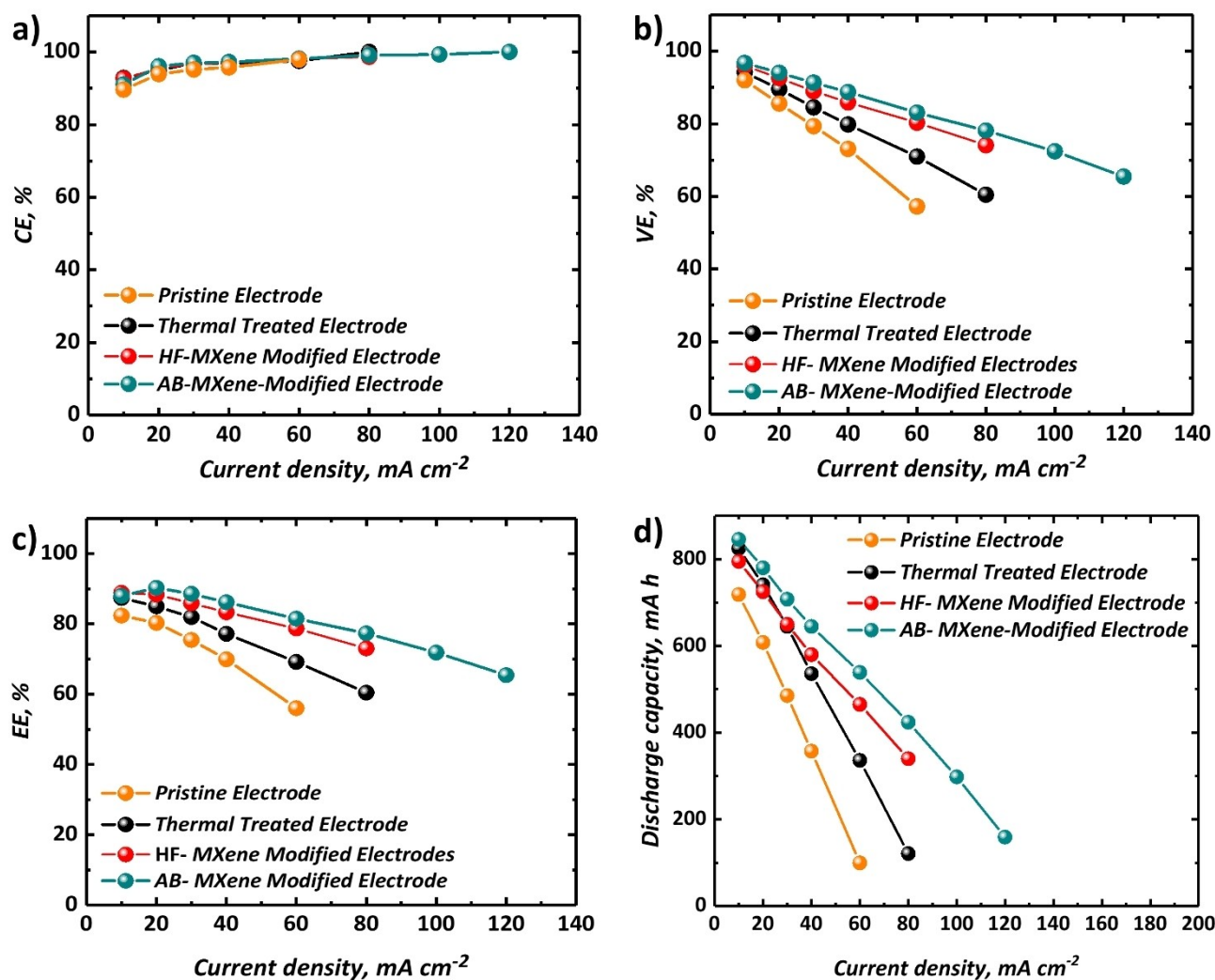
Batteries & Supercaps

Research Article
doi.org/10.1002/batt.202300473

Chemistry
Europe

European Chemical
Societies Publishing

Figure 5. Comparison of VRFB performance using pristine, thermal treated, and MXene modified electrodes (etched with HF and NH_4HF_2: AB): (a) coulombic efficiency (CE); (b) voltage efficiency (VE); (c) energy efficiency (EE); and (d) discharge capacity at a range of current densities.

transport capability contributes to increased capacity and overall efficiency of the VRFB.[46,47]

The power density and polarization data obtained for VRFBs using a thermally treated and NH_4HF_2-etched MXene modified negative electrodes at 100% and 50% SOC of VRFB are shown in Figure 6a and Figure S5, respectively. At low current density, charge transfer overpotential loss is the dominant factor whereas at high current density, the effect of mass transport overpotential dominates.[41] The VRFB using the NH_4HF_2-etched MXene modified electrodes have lower overpotential losses compared to the VRFB using a thermally treated negative electrode, confirming the improvement in the VRFB performance. The maximum power density delivered by the VRFB increased by 41% (from 217 mW cm^{-2} to 305 mW cm^{-2}) and 42% (from 149 mW cm^{-2} to 212 mW cm^{-2}) due to MXene modification of the negative electrode, at 100% and 50% SOC, respectively.

EIS was performed on the VRFB using a thermally treated and NH_4HF_2-etched MXene modified negative electrode, at open circuit and at a SOC of 50%. The Nyquist plots obtained

are shown in Figure 6b. The shape of the Nyquist plot indicates two overlapping semi-circles, consistent with previous studies that have associated these semi-circles with the positive and negative electrode reactions.[3,70] Following these previous studies, the EIS data was fitted to a simple equivalent circuit representative of the physical system (shown in Figure 6b). Although alternative equivalent circuits could be used to fit the data, this circuit enables comparison of the behavior of the VRFB with different electrode materials. The ohmic resistance (R_s) and charge transfer resistance (R_{CT}) of the positive and negative electrodes were determined by fitting the data to the equivalent circuit shown in Figure 6b, and the values obtained are shown in Table S1. The ohmic resistance of the cell (R_s) is indicated by the high frequency intercept of the Nyquist plot with the horizontal axis, and the charge transfer resistances (R_{CT}) of the two electrodes are related to the diameter of the overlapping flattened semi-circles.[3,71]

As shown in Figure 6b, the VRFB using a NH_4HF_2-etched MXene modified negative electrode exhibited a slightly lower ohmic resistance R_s (indicated by high frequency intercept) of
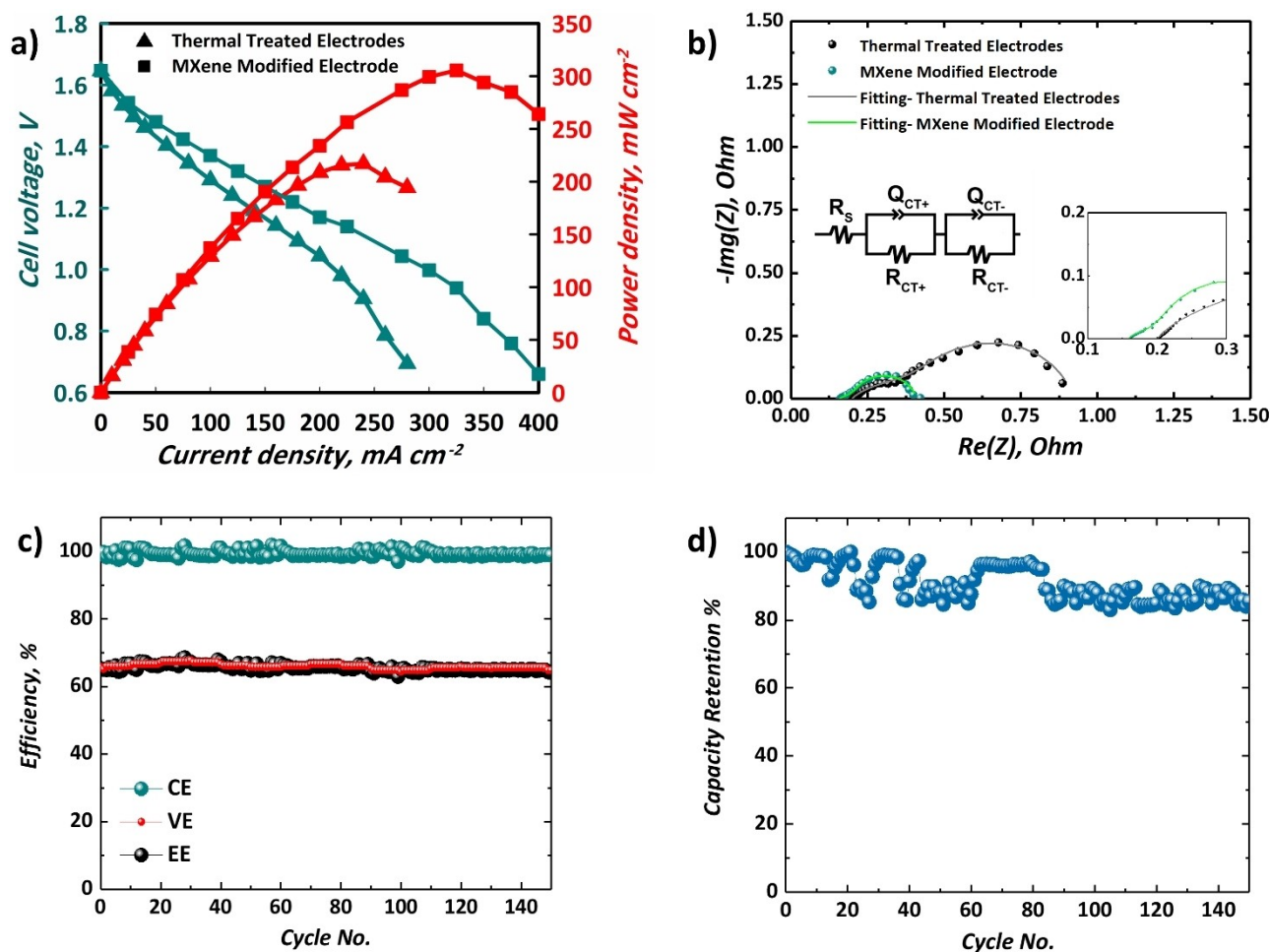
Figure 6. (a) Polarization curves at 100% SOC, (b) EIS at open circuit voltage for VRFB using thermal treated and NH_4HF_2-etched MXene modified electrode; VRFB stability versus cycling with NH_4HF_2-etched MXene modified electrode, including: (c) efficiencies, (d) capacity retention, during 150 cycles of VRFB charge discharge at a current density of 120 mA cm^{-2}.

0.15 Ω, compared to the with the thermal treated electrode. This decrease in ohmic resistance is likely due to an increase in the conductivity of the carbon paper due to the addition of the conductive MXene. A significantly lower charge transfer resistance, indicated by the reduced diameter of the semi-circles, was observed for the VRFB using the NH_4HF_2-etched MXene modified negative electrode. The EIS results also revealed that the charge transfer resistance for the negative electrode R_{CT-} (assumed to be the larger of the overlapping semicircles[3,72] was significantly decreased for the MXene modified electrode from 0.65 Ω to 0.17 Ω (Table S1). The observations from EIS are consistent with the polarization, charge-discharge, and CV data. It is clear that use of a MXene modified electrode improves the overall performance of the negative electrode by enhancing the electrochemical activity and providing more active sites for the vanadium redox reaction.

In addition to VRFB performance enhancement, it is also important to evaluate the NH_4HF_2-etched MXene modified electrode stability during cycling at high current density. The VRFB was operated for 150 charge-discharge cycles at current density of 120 mA cm^{-2}. The VRFB efficiencies and capacity

retention during cycling are summarized in Figure 6c and d, respectively. The results confirm the electrode stability at high current density, as there was no decrease in the voltage efficiency or energy efficiency, which remained around 66–70%. The capacity of the battery decreased slightly (Figure 6d) but stabilized after 90 cycles and maintained a capacity retention of 83–86% between cycles 100 and 150. The coulombic efficiency was also stable at close to 100% throughout the 150 charge-discharge cycles. The charge-discharge voltage curves for cycles, 1, 50, 100 and 150 are shown in Figure S6, demonstrating the stability of the electrodes. The slight decrease in capacity is likely due to vanadium crossover leading to an imbalance in the VRFB electrolytes[73] rather than a decrease in electrode activity.

The wettability of porous electrodes affects electrolyte diffusion and access to the active sites on the electrode surface. The low contact angle of the MXene modified electrode (Figure 2b) confirms their higher wettability. In addition, the presence of the more open structure (Figure 2c), with larger interlayer spacing of the NH_4HF_2-etched MXene provides greater electrochemically active surface, increasing the active area of

the electrode. Based on the CV experiment, NH$_4$HF$_2$-etched MXene modified electrode demonstrated the highest kinetics for the V^{2+}/V^{3+} redox reaction, indicated by the lower peak separation and higher peak current. The higher VRFB performance is thus related to the better wettability, higher electrical conductivity, and electrocatalytic activity of the NH$_4$HF$_2$-etched MXene nanostructures, which provides more active sites on the electrode surface and better kinetics for the V^{2+}/V^{3+} redox reaction.

Long-term stability of VRFB is essential for renewable energy storage applications, and thus any proposed material modification must also demonstrate long-term stability. To evaluate the stability of the thermally treated and NH$_4$HF$_2$-etched MXene modified electrode, the charge-discharge tests over 1000 cycles were conducted at a current density of 80 mA cm^{-2} (Figure 7).

The VRFB assembled with the thermal treated negative electrode failed after 500 charge-discharge cycles, with a discharge capacity decay of around 0.2% per cycle (i.e., a decrease from 182 mA h to 4 mA h over 500 cycles). The initial discharge capacity for the NH$_4$HF$_2$-etched MXene modified electrode was recorded at 420 mA h and reduced to a final capacity of 205 mA h after 1000 cycles, corresponding to a discharge capacity decay of 0.05% per cycle. This is at the low end of the range of capacity decay rates reported for VRFB,[73] and one of the lowest ever reported for a VRFB using a Nafion membrane. The results clearly demonstrate that a significantly better capacity retention can be achieved with a NH$_4$HF$_2$-etched MXene modified negative electrode. Previous work[40] has shown that MXene particles prepared by drop casting and vacuum drying at 50 °C remain attached to the carbon fibers of the electrode after VRFB cycling. The cycling behavior observed in this study confirms that this method is sufficient for ensuring stability of the MXene particles.

Previous studies have indicated that the mechanism of capacity decay is caused by a combination of effects, including vanadium crossover (a function of the membrane material), and electrode degradation.[69] The improvement in the capacity retention by the MXene modified electrode suggests that the activity of this electrode material is more stable than the thermally treated carbon paper. However, since the voltage efficiency of the thermal treated carbon paper is stable, further work is needed to investigate the mechanism of capacity loss, and how this is impacted by the MXene modification. The coulombic efficiency, energy efficiency, and discharge capacity retention over 1000 cycles are presented in Figure S7.

A discharge capacity retention of 50% was reached after around 750 cycles, and the discharge capacity was stable from 750 to 1000 cycles (Figure 7a and Figure S7). The fluctuations in discharge capacity are due to the charge-discharge protocol, as has been reported in similar previous studies.[6,74] As a cut-off voltage protocol was used for the battery cycling, the SOC of the electrolyte can vary between cycles, leading to the observed fluctuation in capacity.

The results show that the NH$_4$HF$_2$-etched MXene modified negative electrode is stable during VRFB cycling. The VRFB with the NH$_4$HF$_2$-etched MXene modified negative electrode exhibited higher voltage efficiency and energy efficiency throughout long-term cycling compared to the conventional thermally treated carbon paper electrode. To the best of our knowledge, this current study presents results with the best stability metrics for MXene modified electrodes over long-term cycling. Previously, a HF-etched MXene decorated electrode has demonstrated 48% discharge capacity retention after 500 VRFB charge-discharge cycles.[14] This corresponds to a capacity decay rate of 0.1% per cycle, significantly higher than the 0.05% per cycle achieved in this study. Furthermore, most studies have used a graphite felt electrode material, which are known to have higher structural integrity when compared with carbon paper.[10,75] The different exfoliation method (NH$_4$HF$_2$-etched) used for obtaining MXene from MAX phase may also explain the improved VRFB stability obtained in this study, compared to HF-etched MXene decorated on graphite felt previously reported.[14,40] The larger interlayer spacing of NH$_4$HF$_2$-etched
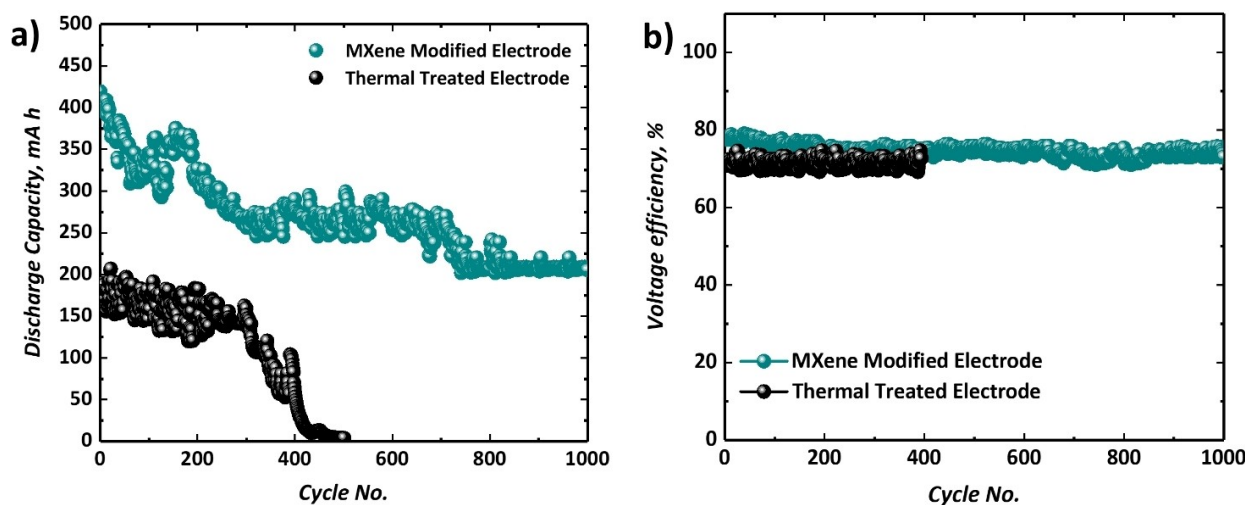

Figure 7. Comparing cycling stability for the thermal treated and NH$_4$HF$_2$-etched MXene modified electrode, by the: (a) discharge capacity, (b) VE, over 1000 cycles at an 80 mA cm^{-2} current density.

Batteries & Supercaps

Research Article
doi.org/10.1002/batt.202300473

Chemistry
Europe

European Chemical
Societies Publishing

MXene compared to HF-etched MXene can improve the transport of vanadium ions to and from the electrode, which can increase the overall efficiency and stability of the VRFB.[46,47] Additionally, the use of NH_4HF_2 as an etchant can also result in MXene layers with fewer defects and a more uniform thickness, which can further improve the electrochemical performance of the electrode.[46]

Conclusions

In this study, the NH_4HF_2-etched MXene was characterized with an increased interlayer spacing that allows for better ion transport and higher capacity retention, which is beneficial for electrochemical energy storage purposes. Ammonium bifluoride is also a more environmentally friendly alternative to HF and is easier to handle when considering scale up of the production process.

The synthesized MXene nanostructures was used to modify a thermally treated carbon paper for use as the negative electrode in a VRFB. The VRFB performance using pristine, thermally treated, and MXene modified (HF-etched and NH_4HF_2-etched) carbon paper as the negative electrode were evaluated and compared. The CV results showed that the NH_4HF_2-etched MXene modified electrode has a favorable electrocatalytic behavior towards V^{2+}/V^{3+} redox reaction. The best battery performance was obtained with the NH_4HF_2-etched MXene modified electrode, which is attributed to the electrochemical activity of the MXene for the V^{2+}/V^{3+} reaction, and the wider spaced interlayers within the MXene sheets that increases accessibility to the active sites for the redox reaction.

The energy efficiencies at a current density of $60\,mA\,cm^{-2}$ for the NH_4HF_2-etched MXene modified, thermally treated, and pristine electrodes were 81.5%, 69%, and 56%, respectively. The energy efficiency of the VRFB thus increased by 25.5% when using a NH_4HF_2-etched MXene-modified negative electrode, by 12.5% with a thermal-treated MXene-modified electrode, and by 4% with an HF-etched MXene-modified electrode, in comparison to the pristine electrode. In addition, the maximum current density for charge-discharge of the VRFB increased from $80\,mA\,cm^{-2}$ to $120\,mA\,cm^{-2}$ when MXene nanostructures were decorated on the thermally treated carbon paper negative electrode. This is highest current density reported to date for charge-discharge of VRFBs using carbon paper-based electrodes. The NH_4HF_2-etched MXene modified electrode enabled a 41% increase in the maximum power density of the battery at a 100% SOC (from $217\,mW\,cm^{-2}$ to $305\,mW\,cm^{-2}$).

Galvanostatic cycling of the VRFB using a NH_4HF_2-etched MXene modified electrode was conducted at current densities of 80 and $120\,mA\,cm^{-2}$ to evaluate the durability of the electrode. The results clearly demonstrate the electrode stability as the voltage efficiency and energy efficiency values showed negligible drop throughout these experiments. An 85% capacity retention after 150 cycles was recorded at the highest current density of $120\,mA\,cm^{-2}$. The larger interlayer spacing of NH_4HF_2-etched MXene improved the transport of vanadium

ions to and from the electrode, which increased the overall efficiency and stability of the VRFB.

The findings demonstrate the influence of MXene incorporation by decorating them on thermally treated carbon paper. This led to significantly improved VRFB performance based on the increased electrical conductivity, associated electrochemical activity, and wettability of the negative electrode. These factors provided extra active sites for enhanced V^{2+}/V^{3+} redox reaction and lowered system overpotentials. Consequently, a higher battery power density was achieved due to increased operating current density and voltage efficiency that could significantly reduce the battery stack size for a higher target power output.

Conflict of Interests

The authors declare no conflict of interest.

Data Availability Statement

The data that support the findings of this study are available from the corresponding author upon reasonable request.

[1] A. Pasadakis-Kavounis, F. Arslan, M. Radmer Almind, D. Aili, J. Hjelm, *Batteries & Supercaps* **2023**, *6*, e202300176.
[2] A. Fetyan, M. O. Bamgbopa, A. Andisetiawan, A. Alhammadi, R. A. Susantyoko, *Batteries & Supercaps* **2023**, *6*, e202300301.
[3] M. Pahlevaninezhad, E. E. Miller, L. Yang, L. S. Prophet, A. Singh, T. Storwick, M. Pahlevani, M. A. Pope, E. P. L. Roberts, *ACS Appl. Energ. Mater.* **2023**, *6*, 6505–6517.
[4] Z. Huang, A. Mu, L. Wu, B. Yang, Y. Qian, J. Wang, *ACS Sustainable Chem. Eng.* **2022**, *10*, 7786–7810.
[5] X. Wang, R. K. Gautam, J. Jiang, *Batteries & Supercaps* **2022**, *5*, e202200298.
[6] M. Pahlevaninezhad, M. Pahlevani, E. P. L. Roberts, *J. Power Sources.* **2022**, *529*, 231271.
[7] Y. Zhou, L. Liu, Y. Shen, L. Wu, L. Yu, F. Liang, J. Xi, *Chem. Commun.* **2017**, *53*, 7565–7568.
[8] A. Vala Mizrak, J. C. Ehring, M. Shekhirev, R. W. Lord, B. Aküzüm, P. Singh, Y. Gogotsi, E. C. Kumbur, *Batteries & Supercaps* **2022**, *5*, e202200321.
[9] L. Wei, T. S. Zhao, L. Zeng, X. L. Zhou, Y. K. Zeng, *Appl. Energy.* **2016**, *180*, 386–391.
[10] Y. Liu, Y. Shen, L. Yu, L. Liu, F. Liang, X. Qiu, J. Xi, *Nano Energy.* **2018**, *43*, 55–62.
[11] B. Li, M. Gu, Z. Nie, Y. Shao, Q. Luo, X. Wei, X. Li, J. Xiao, C. Wang, V. Sprenkle, et al., *Nano Lett.* **2013**, *13*, 1330–1335.
[12] X. L. Zhou, Y. K. Zeng, X. B. Zhu, L. Wei, T. S. Zhao, *J. Power Sources.* **2016**, *325*, 329–336.
[13] Z. He, Y. Lv, T. Zhang, Y. Zhu, L. Dai, S. Yao, W. Zhu, L. Wang, *Chem. Eng. J.* **2022**, *427*, 131680.

Batteries & Supercaps

Research Article
doi.org/10.1002/batt.202300473

Chemistry Europe
European Chemical
Societies Publishing

[14] L. Wei, C. Xiong, H. R. Jiang, X. Z. Fan, T. S. Zhao, *Energy Storage Mater.* **2020**, *25*, 885–892.

[15] K. J. Kim, M. S. Park, Y. J. Kim, J. H. Kim, S. X. Dou, M. Skyllas-Kazacos, *J. Mater. Chem. A.* **2015**, *3*, 16913–16933.

[16] K. V. Greco, A. Forner-Cuenca, A. Mularczyk, J. Eller, F. R. Brushett, *ACS Appl. Mater. Interfaces.* **2018**, *10*, 44430–44442.

[17] J. M. Jeong, K. Il Jeong, J. H. Oh, Y. S. Chung, S. S. Kim, *Appl. Mater. Today.* **2021**, *24*, 101139.

[18] D. S. Aaron, Q. Liu, Z. Tang, G. M. Grim, A. B. Papandrew, A. Turhan, T. A. Zawodzinski, M. M. Mench, *J. Power Sources.* **2012**, *206*, 450–453.

[19] R. M. Darling, M. L. Perry, *J. Electrochem. Soc.* **2014**, *161*, A1381–A1387.

[20] P. Mazúr, J. Mrlík, J. Beneš, J. Pocedič, J. Vrána, J. Dundálek, J. Kosek, *J. Power Sources.* **2018**, *380*, 105–114.

[21] A. Kaur, K. Il Jeong, S. Su Kim, J. Woo Lim, *Compos. Struct.* **2022**, *290*, 115546.

[22] L. Yue, W. Li, F. Sun, L. Zhao, L. Xing, *Carbon* **2010**, *48*, 3079–3090.

[23] Z. He, Y. Jiang, W. Meng, F. Jiang, H. Zhou, Y. Li, J. Zhu, L. Wang, L. Dai, *Appl. Surf. Sci.* **2017**, *423*, 111–118.

[24] J. Z. Chen, W. Y. Liao, W. Y. Hsieh, C. C. Hsu, Y. S. Chen, *J. Power Sources.* **2015**, *274*, 894–898.

[25] K. E. Kim, E. Chandrasekar, H. Y. Lam, *Race Soc. Probl.* **2014**, *6*, 4–14.

[26] B. Sun, M. Skyllas-Kazacos, *Electrochim. Acta.* **1992**, *37*, 1253–1260.

[27] L. Wei, T. S. Zhao, G. Zhao, L. An, L. Zeng, *Appl. Energy.* **2016**, *176*, 74–79.

[28] A. Di Blasi, O. Di Blasi, N. Briguglio, A. S. Aricò, D. Sebastián, M. J. Lázaro, G. Monforte, V. Antonucci, *J. Power Sources.* **2013**, *227*, 15–23.

[29] B. Hou, X. Cui, Y. Chen, *Solid State Ionics.* **2018**, *325*, 148–156.

[30] J. Vázquez-Galván, C. Flox, J. R. Jervis, A. B. Jorge, P. R. Shearing, J. R. Morante, *Carbon* **2019**, *148*, 91–104.

[31] C. N. Sun, F. M. Delnick, D. S. Aaron, A. B. Papandrew, M. M. Mench, T. A. Zawodzinski, *ECS Electrochem. Lett.* **2013**, *2*, 43–46.

[32] S. Mehboob, G. Ali, S. Abbas, K. Y. Chung, H. Y. Ha, *J. Ind. Eng. Chem.* **2019**, *80*, 450–460.

[33] M. Naguib, M. W. Barsoum, Y. Gogotsi, *Adv. Mater.* **2021**, *33*, 1–10.

[34] Q. Zhu, J. Li, P. Simon, B. Xu, *Energy Storage Mater.* **2021**, *35*, 630–660.

[35] Q. Lu, C. Liu, Y. Zhao, W. Pan, K. Xie, P. Yue, G. Zhang, A. Omar, L. Liu, M. Yu, et al., *SusMat* **2023**, *3*, 471–497.

[36] M. Naguib, M. Kurtoglu, V. Presser, J. Lu, J. Niu, M. Heon, L. Hultman, Y. Gogotsi, M. W. Barsoum, *Adv. Mater.* **2011**, *23*, 4248–4253.

[37] S. Xiao, Y. Zheng, X. Wu, M. Zhou, X. Rong, L. Wang, Y. Tang, X. Liu, L. Qiu, C. Cheng, *Small.* **2022**, *18*, 1–30.

[38] H. Fan, W. Luo, S. Dou, Z. Zheng, *SmartMat.* **2023**, *4*, 1–30.

[39] X. Li, Z. Huang, C. E. Shuck, G. Liang, Y. Gogotsi, C. Zhi, *Nat. Chem. Rev.* **2022**, *6*, 389–404.

[40] M. Jing, X. Li, H. Yu, X. An, Z. Liu, A. Zhang, X. Qin, C. Li, D. Fang, *Chem. Eng. J.* **2023**, *455*, 140789.

[41] A. V. Mizrak, S. Uzun, B. Akuzum, L. Agartan, Y. Gogotsi, E. C. Kumbur, *J. Electrochem. Soc.* **2021**, *168*, 090518.

[42] T. Kobayashi, Y. Sun, K. Prenger, D. E. Jiang, M. Naguib, M. Pruski, *J. Phys. Chem. C.* **2020**, *124*, 13649–13655.

[43] P. Lakhe, E. M. Prehn, T. Habib, J. L. Lutkenhaus, M. Radovic, M. S. Mannan, M. J. Green, *Ind. Eng. Chem. Res.* **2019**, *58*, 1570–1579.

[44] K. Arole, J. W. Blivin, S. Saha, D. E. Holta, X. Zhao, A. Sarmah, H. Cao, M. Radovic, J. L. Lutkenhaus, M. J. Green, *iScience.* **2021**, *24*, 103403.

[45] L. H. Karlsson, J. Birch, J. Halim, M. W. Barsoum, P. O. Å. Persson, *Nano Lett.* **2015**, *15*, 4955–4960.

[46] J. Halim, M. R. Lukatskaya, K. M. Cook, J. Lu, C. R. Smith, L. Å. Näslund, S. J. May, L. Hultman, Y. Gogotsi, P. Eklund, et al., *Chem. Mater.* **2014**, *26*, 2374–2381.

[47] A. Feng, Y. Yu, F. Jiang, Y. Wang, L. Mi, Y. Yu, L. Song, *Ceram. Int.* **2017**, *43*, 6322–6328.

[48] Y. Wang, N. Chen, B. Zhou, X. Zhou, B. Pu, J. Bai, Q. Tang, Y. Liu, W. Yang, *Nano-Micro Lett.* **2023**, *15*, 1–12.

[49] H. W. Wang, M. Naguib, K. Page, D. J. Wesolowski, Y. Gogotsi, *Chem. Mater.* **2016**, *28*, 349–359.

[50] D. Reed, E. Thomsen, W. Wang, Z. Nie, B. Li, X. Wei, B. Koeppel, V. Sprenkle, *J. Power Sources.* **2015**, *285*, 425–430.

[51] Y. Ahn, D. Kim, *Energy Storage Mater.* **2020**, *31*, 105–114.

[52] M. Skyllas-Kazacos, L. Cao, M. Kazacos, N. Kausar, A. Mousa, *ChemSusChem.* **2016**, *9*, 1521–1543.

[53] C. Zhao, Q. Wang, H. Zhang, S. Passerini, X. Qian, *ACS Appl. Mater. Interfaces.* **2016**, *8*, 15661–15667.

[54] H. Wang, Y. Wu, J. Zhang, G. Li, H. Huang, X. Zhang, Q. Jiang, *Mater. Lett.* **2015**, *160*, 537–540.

[55] A. Feng, Y. Yu, Y. Wang, F. Jiang, Y. Yu, L. Mi, L. Song, *Mater. Des.* **2017**, *114*, 161–166.

[56] A. Lipatov, M. Alhabeb, M. R. Lukatskaya, A. Boson, Y. Gogotsi, A. Sinitskii, *Adv. Electron. Mater.* **2016**, *2*, 1600255.

[57] J. Halim, K. M. Cook, M. Naguib, P. Eklund, Y. Gogotsi, J. Rosen, M. W. Barsoum, *Appl. Surf. Sci.* **2016**, *362*, 406–417.

[58] W. Y. Chen, X. Jiang, S. N. Lai, D. Peroulis, L. Stanciu, *Nat. Commun.* **2020**, *11*, 1–10.

[59] A. Tanvir, P. Sobol, A. Popelka, Miroslav Mrlik, M. Micusik, J. Prokes, I. Krupa, *Polymer* **2019**, *11*, 1272.

[60] M. Mičušík, M. Šlouf, A. Stepura, Y. Soyka, E. Ovodok, M. Procházka, M. Omastová, *Appl. Surf. Sci.* **2023**, *610*, 155351.

[61] L. Geng, P. Zhu, Y. Wei, R. Guo, C. Xiang, C. Cui, Y. Li, *Cellulose* **2019**, *26*, 2833–2847.

[62] W. Y. Chen, X. Jiang, S. N. Lai, D. Peroulis, L. Stanciu, *Nat. Commun.* **2020**, *11*, 1–10.

[63] S. A. Shah, T. Habib, H. Gao, P. Gao, W. Sun, M. J. Green, M. Radovic, *Chem. Commun.* **2017**, *53*, 400–403.

[64] L. Geng, P. Zhu, Y. Wei, R. Guo, C. Xiang, C. Cui, Y. Li, *Cellulose* **2019**, *26*, 2833–2847.

[65] S. Yazdanparast, S. Soltanmohammad, A. Fash-White, G. J. Tucker, G. L. Brennecka, *ACS Appl. Mater. Interfaces.* **2020**, *12*, 20129–20137.

[66] D. chuan Zuo, S. chao Song, C. sheng An, L. bo Tang, Z. jiang He, J. chao Zheng, *Nano Energy.* **2019**, *62*, 401–409.

[67] M. R. Lukatskaya, O. Mashtalir, C. E. Ren, Y. Dall'Agnese, P. Rozier, P. L. Taberna, M. Naguib, P. Simon, M. W. Barsoum, Y. Gogotsi, *Science.* **2013**, *341*, 1502–1505.

[68] Y. Li, J. Parrondo, S. Sankarasubramanian, V. Ramani, *J. Phys. Chem. C.* **2019**, *123*, 6370–6378.

[69] X. Z. Yuan, C. Song, A. Platt, N. Zhao, H. Wang, H. Li, K. Fatih, D. Jang, *Int. J. Energy Res.* **2019**, *43*, 6599–6638.

[70] Q. Yang, J. Xu, B. Cao, X. Li, *PLoS One.* **2017**, *12*, 1–13.

[71] L. Wu, J. Wang, Y. Shen, L. Liu, J. Xi, *Phys. Chem. Chem. Phys.* **2017**, *19*, 14708–14717.

[72] K. Percin, B. van der Zee, M. Wessling, *ChemElectroChem.* **2020**, *7*, 2165–2172.

[73] K. E. Rodby, T. J. Carney, Y. Ashraf Gandomi, J. L. Barton, R. M. Darling, F. R. Brushett, *J. Power Sources.* **2020**, *460*, 227958.

[74] Y. Jiang, G. Cheng, Y. Li, Z. He, J. Zhu, W. Meng, L. Dai, L. Wang, *Chem. Eng. J.* **2021**, *415*, 129014.

[75] H. R. Jiang, W. Shyy, L. Zeng, R. H. Zhang, T. S. Zhao, *J. Mater. Chem. A.* **2018**, *6*, 13244–13253.